Available online at www.sciencedirect.com
SCIENCE DIRECT®
Journal of Nuclear Materials 354 (2006) 66–84
journal of nuclear materials
www.elsevier.com/locate/jnucmat

Stereological evolution of the rim structure in PWR-fuels at prolonged irradiation: Dependencies with burn-up and temperature

J. Spino [a,*], A.D. Stalios [b], H. Santa Cruz [a], D. Baron [c]

[a] European Commission, Joint Research Centre, Institute for Transuranium Elements, P.O. Box 2340, D-76125 Karlsruhe, Germany
[b] European Commission, DG RTD, Industrial Technologies-Materials, CDMA 00/168, Rue du Champ de Mars 21, B-1049 Brussels, Belgium
[c] Electricité de France (EDF), Research and Development, CEA Cadarache, DEC/SESC, 13108 Saint-Paul-Lez-Durance cedex, France

Received 15 November 2005; accepted 15 February 2006

Abstract

The stereology of the rim-structure was studied for PWR-fuels up to the ninth irradiation cycle, achieving maximum local burn-ups of 240 GWd/tM and beyond. At intermediate radial positions ($0.55 < r/r_0 < 0.7$), a small increase of the pore and grain size of recrystallized areas was found, which is attributed to the increase of the irradiation temperatures in the outer half-pellet-radius due to deterioration of the thermal conductivity. In the rim-zone marked pore coarsening and pore-density-drop occur on surpassing the local burn-up of 100 GWd/tM, associated with cavity fractions of ≈0.1. Above this threshold the porosity growth rate drops and stabilizes at a value nearing the matrix-gas swelling-rate (≈0.6%/10 GWd/tM). The rim-cavity coarsening shows ingredients of both Ostwald-ripening and coalescence mechanisms. Despite individual pore-contact events, no clusters of interconnected pores were observed up to maximum pore fractions checked (≈0.24). The rim-pore-structure is found to be well represented in its lower bound by the model system of random penetrable spheres, with percolation threshold at $\phi_c = 0.29$. Rim-cavities are expected to remain closed at least up to this limit.

1. Introduction

Fundamental stereological parameters of the so-called rim-structure that develops at the periphery of PWR-fuels at high burn-ups were provided first in [1] for the average burn-up range 40–67 GWd/tM.

Under the conditions of [1] where the transformation affected only a band of 200–250 μm at the pellet edge (i.e., at most 5% of the pellet radius), it was reported that a new population of pores was created in the transformed zone, with a different aspect compared to the fabrication pores but with similar diameters (mono-modal distribution peaked at ~1 μm); the fractional porosity and the pore-density increased exponentially towards the pellet edge, following approximately the radial burn-up profile [1]. The new pores, of typical faceted nature, appeared invariably surrounded by (few) layers of recrystallized (sub)grains with most sizes comprised in the range 0.15–0.45 μm. The description supplied in [1] assumed thus localized recrystallization of the matrix around pores. Although alternative

* Corresponding author. Tel.: +49 7247 951 233; fax: +49 7247 951 591.
E-mail address: jose.spino@itu.fzk.de (J. Spino).

0022-3115/$ - see front matter © 2006 Elsevier B.V. All rights reserved.
doi:10.1016/j.jnucmat.2006.02.095

explanations were given later in the literature suggesting the irradiation-induced restructuring of the matrix to initiate also at prior grain boundaries [2,3], crack-surfaces [4] or fabrication pores [3,4], the more frequent observation within the high burn-up zone remains that of faceted pores with localized recrystallized surroundings, occasionally, also in coexistence with the original grain boundaries [5].

Evidence provided by us in later works suggested the rim-pore configuration to remain closed up to relatively large porosity fractions (≈25%) [6,7]. For fuels irradiated up to average burn-ups of 60–70 GWd/tM, therefore exhibiting maximum pellet-edge porosity of ~15% [1], full retention of occluded gas in the cavities would be ensured. However, the question arises in how far the rim structure would keep its original (closed) characteristics, e.g. on achieving burn-ups near and above 100 GWd/tM, when the porosity would eventually exceed 25% [7,8] and when, due to deeper penetration into the fuel, the transformed zone would become progressively affected by thermal processes.

In an attempt to provide answers to these questions the stereology of the high burn-up transformed zone was studied in detail for a fuel with roughly 100 GWd/tM average burn-up, analysing limits for pore coarsening and subgrain-growth, as well as possible trends in the percolation threshold.

2. Experimental

2.1. Fuel characteristics

Similar to the samples described in [1], the fuel cross section studied in this work corresponds to the maximum power position of a standard PWR fuel rod irradiated in a commercial power reactor. The burn-up assigned, 98 GWd/tM, corresponds to the pellet-average value at this position. Typical fabrication parameters and a simplified irradiation history along the 9 cycles in the reactor are given in Table 1, as corresponding to data published in [9]. Other fuels with lower extraction burn-ups, also referred to in the present paper, presented similar irradiation history up to the corresponding lower cycles in the reactor (for comparison see Table 1 in [1]).

Table 1
Pellet and rod design data and simplified irradiation history of the PWR-fuels treated in this work

Fuel pellet and rod nominal data	
Fuel rod diameter (mm)	10.75
Diametral gap (μm)	160–190
Initial ^{235}U-enrichment (wt%)	3.5–4.2
Fuel density (gr/cm^3)	10.45
2D-grain size (linear intercept) (μm)	9–12
Fill gas pressure (He) (bar)	22.5
Cladding	Zr-base alloy

Simplified irradiation history

Irradiation cycle	Cycle average linear power (W/cm)	Cumulative average burn-up (GWd/t M)
1	270–340	15–19
2	260–290	29–37
3	210–230	41–48
4	180–200	51–59
5	170–180	60–67
6	160–170	71–72
7	150–160	78–82
8	140	90
9	140	98

2.2. Quantitative ceramography

The information processed in this paper is based on quantitative ceramographic observations of pore features and grain structure of the irradiated fuels, as previously described in [1]. Independently of their eventual content of gas, the so-called pores in this paper refer to cavities in the material with sizes in the micron and submicron range, as being resolved by optical microscopy and scanning electron microscopy (SEM). Gas bubbles in the nanometer-size range, usually resolved by transmission electron microscopy (TEM), and eventually by high magnification SEM, which represent a minor part of the total cavity volume at high burn-ups, are not taken into account in this work. Similar sample preparation techniques and image analysis methods as in [1] were used. Different compared to [1], where only optical micrographs were used; here also scanning electron micrographs (SEM) were included, which allowed larger precision in the features resolution/detection. The quantitative image analysis was done with the equipment Quantimet 520 operated in automatic and semi-automatic modes. Fields of the micrographs selected implied a measuring area of up to 4000 μm^2. The number of features (pores) detected per individual frame studied ranged between 200 and 400. The operator sensitive detection threshold was adjusted using calibrated micrographs of samples with known porosity.

For the conversion of measured 2 D pore-density data into 3D-values the method of Saltikov for

spherical particles described in the treatise of Underwood [10] was used. The method implies classification of the measured 2D-sizes into 12 (decreasing) class-intervals starting from largest (2D) diameter measured. The value of each interval is correlated with the next (smaller) one by a fixed quotient ($d_i/d_{j=i+1} = 0.7943$). Calculation of the corresponding 3D populations per diameter class, N_{Vi}, is hence done using a linear combination of 12 pregiven coefficients [10]. As in random systems a sine qua non condition is the equivalence of the 2D and 3D porosity fractions [10], congruency of the method is verified when $P = 4/3\pi\sum_i N_{Vi}(d_i/2)^3$ approaches the value of the measured 2D-fractional porosity. $N_V = \sum_i N_{Vi}$ represents the total volume pore density of the given cross section [1]. As seen in the corresponding experimental section, the coincidence between the 2D (measured) and the 3D (derived) porosity fractions was verified for all cross sections of the present work.

Parallel determination of (sub)grain sizes in recrystallized regions of the fuel was done on SEM micrographs of fresh fractured surfaces at magnifications between 2000× and 4000×. This implied certain deformation of the real grain sizes due to inclination of the inspected surfaces (depending on the focusing depth), compared for instance to grain size determinations on micrographs of flat polished/etched samples. For this reason, grain sizes histograms were not constructed using the standard linear intercept method (normally applicable to flat samples), but on counting two maximum chords per each individual grain detected. The same method was applied in [1].

2.3. Hardness tests

Multiple hardness tests (five to ten per radial position) were performed on the fuel with 98 GWd/tM average burn-up, at a load of 0.5 N and at 50-μm steps across the fuel radius, in order to determine the radial variation of this property in correspondence with the porosity profile. Details of the test methodology and influence of parameters like applied load, burn-up, etc. can be found in [6].

3. Local burn-up and irradiation temperature calculations with APOLLO 2 and CYRANO 3 codes

To assign local fuel burn-up and irradiation temperature values to the different regions of the fuel(s) analysed, calculations were performed on the base of the data provided in Table 1, using the APOLLO 2 and CYRANO 3 computer codes, respectively. APOLLO 2 is a neutron code currently used for PWR-fuel assemblies calculations [11].

The CYRANO 3 code is routinely used by EdF designers to perform fuel thermo-mechanical calculations and to check new concepts against safety criteria. As it was designed to meet industrial needs, i.e., aiming to assess the behaviour of up to one eighth of the core, i.e., of up to 8000 rods in the same study, compromises were made between the refinement of the models used and the computing time performance. It has a standard 1.5 dimensional FEM thermo-mechanical kernel enriched by an original relocation model accounting for an hourglass effect [12]. An axial stress–strain equilibrium computation is made at each time step accounting for the axial local contacts. This provides border axial conditions for the radial mechanical equilibrium computation at each axial slice [12]. This is the meaning of the 1.5 dimensional calculations.

The thermal calculations in CYRANO 3 account for the evolution of power generation, and for the local variations of temperature and burn-up. The thermal conductivity includes degradations by burn-up and porosity and, in the cold parts of the fuel, previous to rim-structure formation, by irradiation defects. An ad hoc 'rim' model allows evaluating the local porosity increase related to the high burn-up structure transformation [13]. For the present calculations, however, the here measured porosity-vs.-burn-up correlation was used. For the porosity correction of the thermal conductivity the MacDonald–Weisman [14] model was employed, which depends on the local temperature and on the aspect ratio of the pores (oblate/prolate, spherical). This correction is higher for low temperatures and for spherical pores (rim-case). Under these conditions, it yields similar values as the expression $k/k_0 \sim (1 - P)^{1.5}$ (Schulz model [15], case of spherical pores), which has been proposed in [6] as most appropriate for the rim zone.

4. Results and analysis

4.1. Approximate temperature profiles via CYRANO 3 code

The end-of-cycle temperature profiles of the fuel(s) here treated, according to calculations with the CYRANO 3 code previously described, are summarized in Fig. 1. Congruent with the

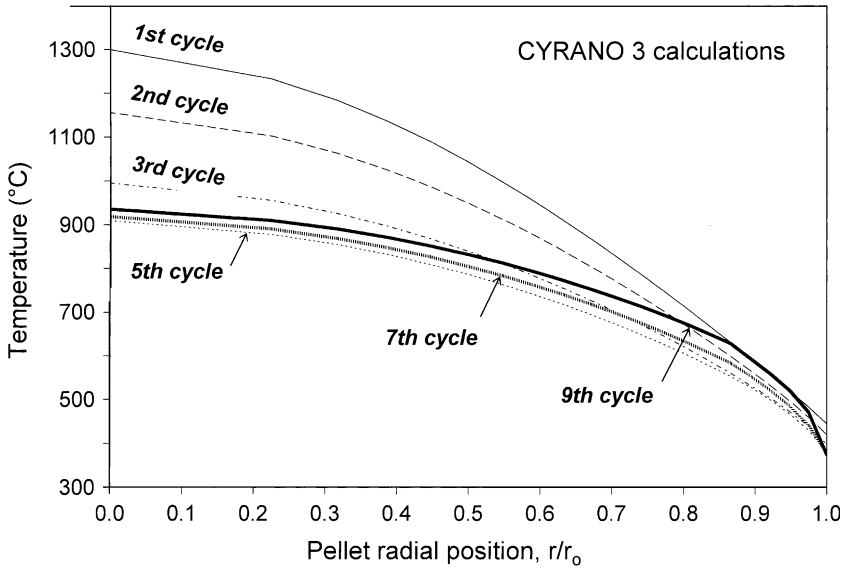

Fig. 1. Approximate temperature profiles of the fuels treated based on CYRANO 3 code calculations, according to the simplified power history of Table 1.

progressive decrease of the linear power (Table 1), the fuel temperatures are shown to decrease with the number of cycles, but only up to the end of the fifth irradiation cycle. For further irradiation cycles, especially from the seventh cycle onwards, the temperatures (at all radial positions) appear to increase again, though more notoriously in the radial range $r/r_0 = 0.6$–0.85 (Fig. 1). Although this effect is moderate (at most 70 °C temperature elevation over the values in the fifth cycle), temperatures in the outer half-radius appear to exceed partially those in the third and even the second cycle (Fig. 1, $r/r_0 \geqslant 0.55$).

The above effect is attributed obviously to the degradation of the thermal conductivity, which, despite recovery at high burn-ups due to defects-healing upon rim-transformation (Ronchi et al. [16]), here also taken into account, remains being important due to porosity and fission products concentration elevations, particularly in outer fuel regions. Due to the simplified power history utilized in the calculations (Table 1), the depicted temperature profiles in Fig. 1 are to be taken just as approximate.

4.2. Porosity-growth processes across the fuel radius

The 2D-porosity fractions of the fuel with average burn-up 98 GWd/tM as determined from optical micrographs (OM) (magnification 500×) and from SEM micrographs (magnification 1000×) are plotted in Fig. 2(top) as a function of the pellet radius. Despite larger scatter of the OM-based data, both types of results depict coincident radial variation. Fig. 2(top) shows also the corresponding local burn-up profile according to APOLLO 2 calculations. The calculated burn-ups agreed within 95% with the values derived from the Nd-concentrations as measured by EPMA. Comparison of this curve with the porosity profile(s) helps recognizing different process regions across the fuel radius.

In the denoted region I of Fig. 2(top) ($r/r_0 \geqslant 0.88$), the remarkable coincidence of the porosity and local burn-up curves allows attributing unambiguously a fully burn-up-controlled process in this zone. This region is assigned as the pure rim. In region II of the figure ($0.68 \leqslant r/r_0 \leqslant 0.88$), the porosity appears to be still controlled by the level of local burn-up, although the light increase of the values at the inner end of the region suggests the existence of a superimposed, eventually thermally-activated pore-growth process at these positions. Within region III of the figure ($0.46 \leqslant r/r_0 \leqslant 0.68$), the gradual decrease of the porosity values below the burn-up conform levels in region II, denotes progressive extinction of the high burn-up effects due to a priori defects-healing and recovery, with tentative quasi-full extinction say at $r/r_0 < 0.55$, where the local temperatures exceeded 800 °C (Fig. 1). According to this rough limit, the high

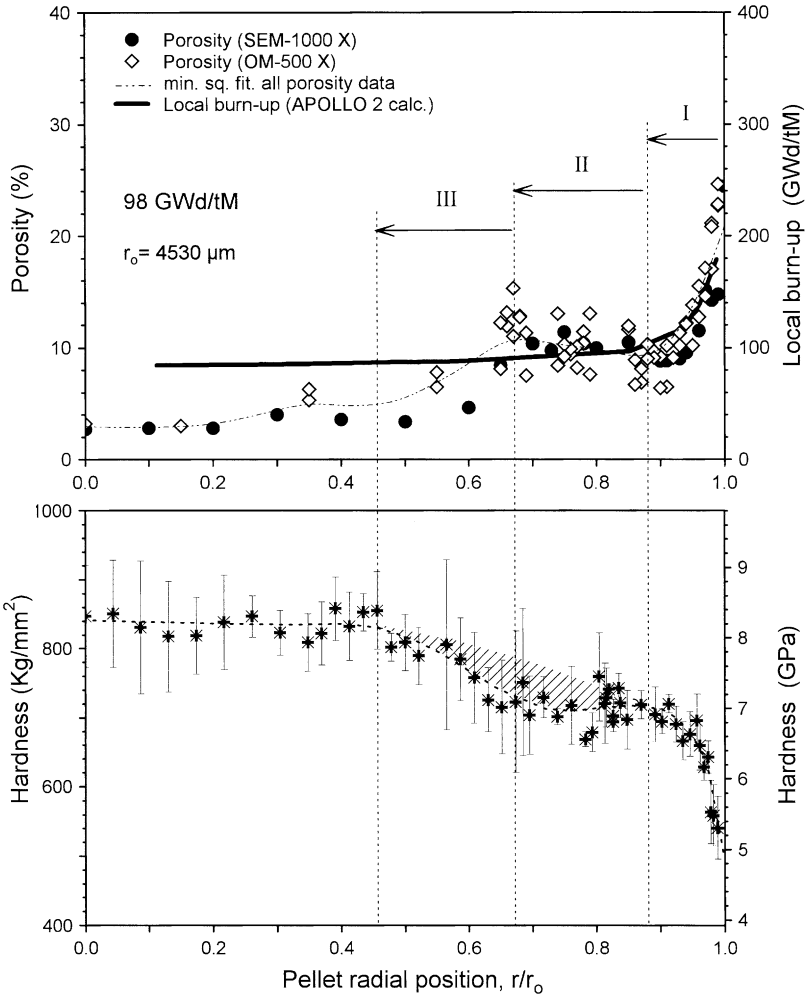

Fig. 2. Fuel with 98 GWd/tM average burn-up. Porosity (2D), local burn-up and hardness radial profiles. Data based on optical (500×) and SEM (1000×) micrographs. Local burn-ups according to APOLLO 2 code calculations.

burn-up region of the fuel in question (ninth irradiation cycle) appears to have involved more than 40% of the pellet radius ($\geqslant$1800 μm-thick peripheral band). This compares with the barely 200–250 μm-wide-zone affected at the end of the fifth irradiation cycle [1].

Fig. 2(bottom) shows the corresponding hardness profile measured according to the brief description in Section 2.3, which is also to be compared with the porosity profile. As previously reported in [6], at a given average burn-up, the variation of the fuel hardness is basically determined by the change of porosity, or in other words, by the change of the load-bearing-area in relation to the dense fuel. It is therefore obvious that both porosity and hardness profiles would lead to the definition of similar regions across the fuel radius, as it is shown in Fig. 2(top and bottom).

However, correlation of the tentative regions marked in Fig. 2 with the underlying microstructure may be not unequivocal since features observed at the end of life may be consequence of different processes that occurred along the irradiation history. Particularly ambiguous seems to be the separation of regions II and III, or the interpretation of the stepwise character of the curves in Fig. 2 around this limit. On the one hand, regions I and III could be seen as branches of two independent rim- or rim-like-transformations, which may have occurred at different irradiation cycles. Equally possible, regions II and III together could be considered as only one extended adjacent-rim (or transition) zone, in the

middle of which a secondary (eventually thermally-driven) cavity-growth mechanism has been established. This could have caused the additional drop of the hardness as it is shown in the shaded area of Fig. 2(bottom). Further evidence presented in next sections seems to reinforce the last hypothesis.

4.3. Derived three-dimensional porosity and pore density data

The 3D-fractional porosity and pore density data deduced by the Saltikov method for the fuel with 98 GWd/tM average burn-up from the measured 2D-data on SEM micrographs (magnification 1000×), as well as the measured average 2D-pore diameters, are plotted in Fig. 3 as a function of the pellet radius. The calculated values, as well as other deduced stereological parameters of the structure are listed in Table 2. Table 2 also contains equivalent derived data for a fuel with 80 GWd/tM (end of seventh cycle), which are employed in Section 4.5. In Fig. 3(top) the measured 2D-pore fractions and the derived 3D-pore fractions are shown to coincide over the whole fuel radius. As mentioned in Section 2.2, this coincidence is indicative of the congruency of the 2D/3D conversion method applied. The figure shows similar radial (process)-zones limits as Fig. 2. Light shift of the limits compared to Fig. 2 is due to the use of only SEM micrographs in the present analysis.

Fig. 3(middle) shows the radial evolution of the extracted 3D-pore density. A particularity of these results is the decrease of the values within the peripheral region I. This behaviour opposes the previous observations at lower burn-ups [1], which indicated an exponential increase of both porosity fraction and pore density towards the pellet edge. As it is seen in the evolution of the average 2D-pore diameter in Fig. 3(bottom), and as will be further analysed in next sections, this reveals a definite pore coarsening mechanism in the burn-up controlled region I, which initiates when local burn-ups exceed the value of ≈100 GWd/tM. In region II, both the constancy of the pore density and the light increase of the porosity fraction (more evident in Fig. 2(top)) suggest a light increase of the cavity size in this zone towards its inner (hotter) side. This can be appreciated also in the average pore size evolution in Fig. 3(bottom) (see also next section). In region III, as indicated in the previous section, the decrease of the porosity fraction and the pore density towards the pellet centre denotes gradual extinction of the high burn-up effects assumedly due to thermal healing of irradiation defects.

4.4. Pore-size distributions throughout the fuel radius

The evolution of the pore populations across the radius in the fuel with 98 GWd/tM average burn-up is described in Fig. 4. The figure shows different sets of curves containing histograms of the 2D/3D-pore size distributions, the cumulative 2D/3D-pore fraction curves and the log–norm fits of the 2D-size distributions, as measured for different radial positions within the three fuel zones marked in Figs. 2 and 3. The 3D-frequency histograms are shown only for two radial positions (i.e., $r/r_0 = 0.5$ and 0.6) (Fig. 4). In general, the aspect of the 3D- and 2D-frequency-distributions was found similar. Also, the cumulative 2D- and 3D-pore-fractions appeared coincident for all cases examined (Fig. 4).

For radial positions $r/r_0 \leqslant 0.6$ (middle of region III towards the fuel centre) relatively narrow pore-size distributions were measured, with peak at around 1 μm-diameter pores (Fig. 4). The cumulative pore fractions in this zone did not exceed 4–5% (see also Figs. 2 and 3(a)). This data, together with the aspect of the pores (predominantly at triple-junctions), suggest cavities in the central zone still responding to the as-fabricated porosity, or to what remains of that after transitory in-pile densification, i.e., after approximately 20 GWd/tM average burn-up. For this kind of fuels, the pore-diameters frequency-distribution in the central zone after e.g. 23 GWd/tM average burn-up peaked at values somewhat above 1 μm [1,17].

For radial positions between $r/r_0 \approx 0.65$ and $r/r_0 \approx 0.9$, and more remarkably in the range $r/r_0 \approx 0.65$–0.7 (transition between regions II and III), the frequency-distributions show a marked asymmetric widening towards larger sizes (positive skewness); the histograms becoming flatter, though still remaining peaked at 1 μm-diameter pores. This obviously leads to an enlarged mean pore size, as already stated in the previous section. Because of the relatively high temperature associated to this region during the ninth cycle (≈800 °C) (Fig. 1), it is believed that the described pore coarsening could have a thermal origin. At the outer end of region II ($r/r_0 \approx 0.9$), the size distributions turn again narrower, at the time that the cumulative porosity achieves a local minimum (Fig. 4). This latter is in

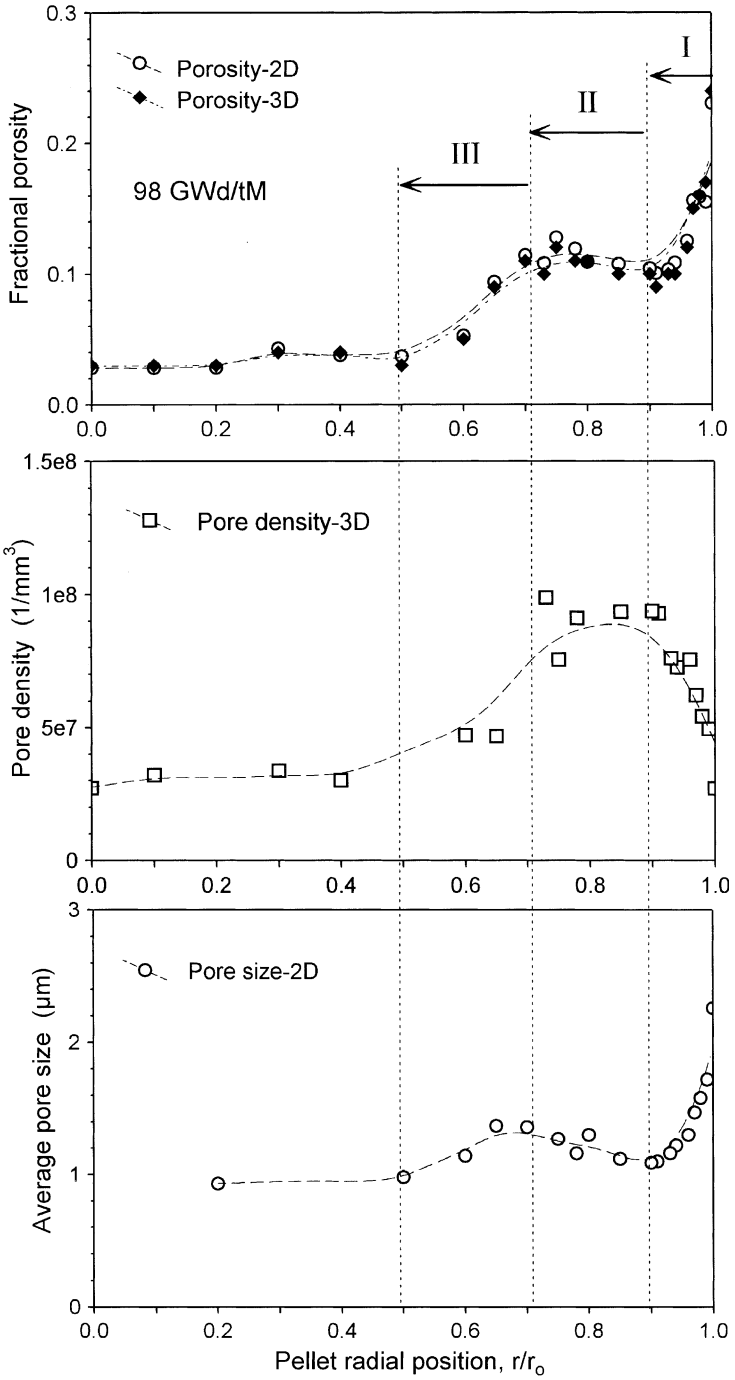

Fig. 3. Fuel with 98 GWd/tM average burn-up. Comparison of 2D and derived 3D porosity data (top). Pore density (3D) and pore size (2D) (middle and bottom, respectively). Data based on SEM (1000×) micrographs.

line with the trend of the porosity profiles shown in Figs. 2 and 3.

Towards the colder pellet edge, congruently with the pore-density decrease shown in the former section, the data of Fig. 4 evidence another important pore coarsening process, involving the whole region I ($r/r_0 \geqslant 0.9$). In this region the pore size distributions become again markedly flatter and widened towards larger sizes, until they finally split into bimodal or tri-modal size distributions at the

Table 2
Quantitative metallography results

Sample burn-up average (GWd/tM)	Radial position (r/r_0)	Measured two-dimensional data		Derived three-dimensional data					
		Porosity P (%)	Pore density (2D) N_A (mm^{-2})	Pore density (3D) N_V (mm^{-3})	Pore diameter		Pore cell size		Pore-to-pore distance (μm) $D_C - D_P$ (μm)
					Average D_A (μm)	Mean D_P (μm)	(Cubic cell) L (μm)	(Spheric cell) D_C (μm)	
98	1.00	24.4	2.60E+04	2.69E+07	2.26	2.54	3.34	4.14	1.60
	0.99	14.8	4.00E+04	4.95E+07	1.72	1.82	2.72	3.38	1.56
	0.98	14.2	6.18E+04	5.43E+07	1.58	1.78	2.64	3.28	1.50
	0.97	15.1	7.24E+04	6.21E+07	1.47	1.69	2.53	3.13	1.45
	0.96	11.5	7.82E+04	7.54E+07	1.30	1.47	2.37	2.94	1.47
	0.94	9.5	7.70E+04	7.25E+07	1.22	1.42	2.40	2.98	1.56
	0.93	9.0	8.25E+04	7.59E+07	1.16	1.37	2.36	2.93	1.56
	0.91	8.9	8.60E+04	9.28E+07	1.10	1.27	2.21	2.74	1.47
	0.90	8.8	9.26E+04	9.37E+07	1.09	1.29	2.20	2.73	1.45
	0.85	10.5	8.76E+04	9.34E+07	1.12	1.30	2.20	2.73	1.43
	0.80	9.9	6.38E+04	5.97E+07	1.30	1.52	2.56	3.17	1.66
	0.78	10.4	9.30E+04	9.10E+07	1.16	1.36	2.22	2.76	1.40
	0.75	11.4	8.09E+04	7.54E+07	1.27	1.48	2.37	2.94	1.46
	0.73	9.8	8.62E+04	9.87E+07	–	–	2.16	2.68	2.68
	0.70	10.4	6.33E+04	6.15E+07	1.36	1.53	2.53	3.14	1.62
	0.65	8.4	4.87E+04	4.68E+07	1.37	1.57	2.78	3.44	1.88
	0.60	4.7	3.67E+04	4.70E+07	1.14	1.29	2.77	3.44	2.15
	0.50	3.3	3.87E+04	5.46E+07	0.98	1.09	2.64	3.27	2.18
80	1.00	14.3	–	–	–	–	–	–	–
	0.99	14.1	6.69E+04	4.37E+07	–	1.83	2.84	3.52	1.69
	0.98	12.9	9.82E+04	8.10E+07	–	1.45	2.31	2.87	1.42
	0.97	11.1	1.11E+05	1.04E+08	–	1.27	2.12	2.63	1.37
	0.96	11.0	1.00E+05	9.08E+07	–	1.32	2.23	2.76	1.44
	0.95	10.7	1.14E+05	1.11E+08	–	1.22	2.08	2.58	1.35
	0.94	10.0	1.00E+05	9.50E+07	–	1.26	2.19	2.72	1.46
	0.93	9.6	9.92E+04	9.57E+07	–	1.24	2.19	2.71	1.47
	0.92	10.2	9.47E+04	8.62E+07	–	1.31	2.26	2.81	1.49
	0.75	9.2	8.44E+04	7.65E+07	–	1.32	2.36	2.92	1.60
	0.50	6.4	6.01E+04	5.51E+07	–	1.30	2.63	3.26	1.96
	0.25	5.1	4.11E+04	3.48E+07	–	1.41	3.06	3.80	2.39
	0	4.9	2.19E+04	1.38E+07	–	1.89	4.17	5.17	3.28

Measured 2D- and derived 3D-data. Fuels with 80 and 98 GWd/tM average burn-ups (ends of seventh and ninth cycles).

outermost positions ($r/r_0 = 0.99$ and $r/r_0 = 1$), with the mean size of each new pore population appearing at roughly a factor 2 or 3 of that of the previous population (Fig. 4). Obviously, the mean pore size becomes greatly increased. At radial position $r/r_0 = 1$, it doubles the value of that at position $r/r_0 = 0.9$ (see Table 2). At the outermost radial positions the major contribution to the fractional porosity arises thus from the largest pores (sizes >4 μm). Although more abundant, pores with diameters around or below 1 μm contribute only slightly to the cavity volume fraction (Fig. 4).

It is to note that asymmetric pore size distributions with positive skewness (tail oriented towards larger sizes), like those invariably observed in this study (Fig. 4), constitute a typical sign of bubble coarsening processes governed by coalescence (e.g. He in metals) [18,19]. The other important coarsening mechanism assigned to gas-bubbles in solids, usually referred in the literature as the Ostwald-ripening [20,21], i.e., this applying to cavities (or precipitates) that grow at expense of the smaller ones due to concentration gradients in the matrix (diffusional solute segregation), definitely show size-distributions with negative skewness (asymmetric tail oriented to smaller sizes). More about the eventual applicability of one or the other mechanism to the rim case is discussed in next sections.

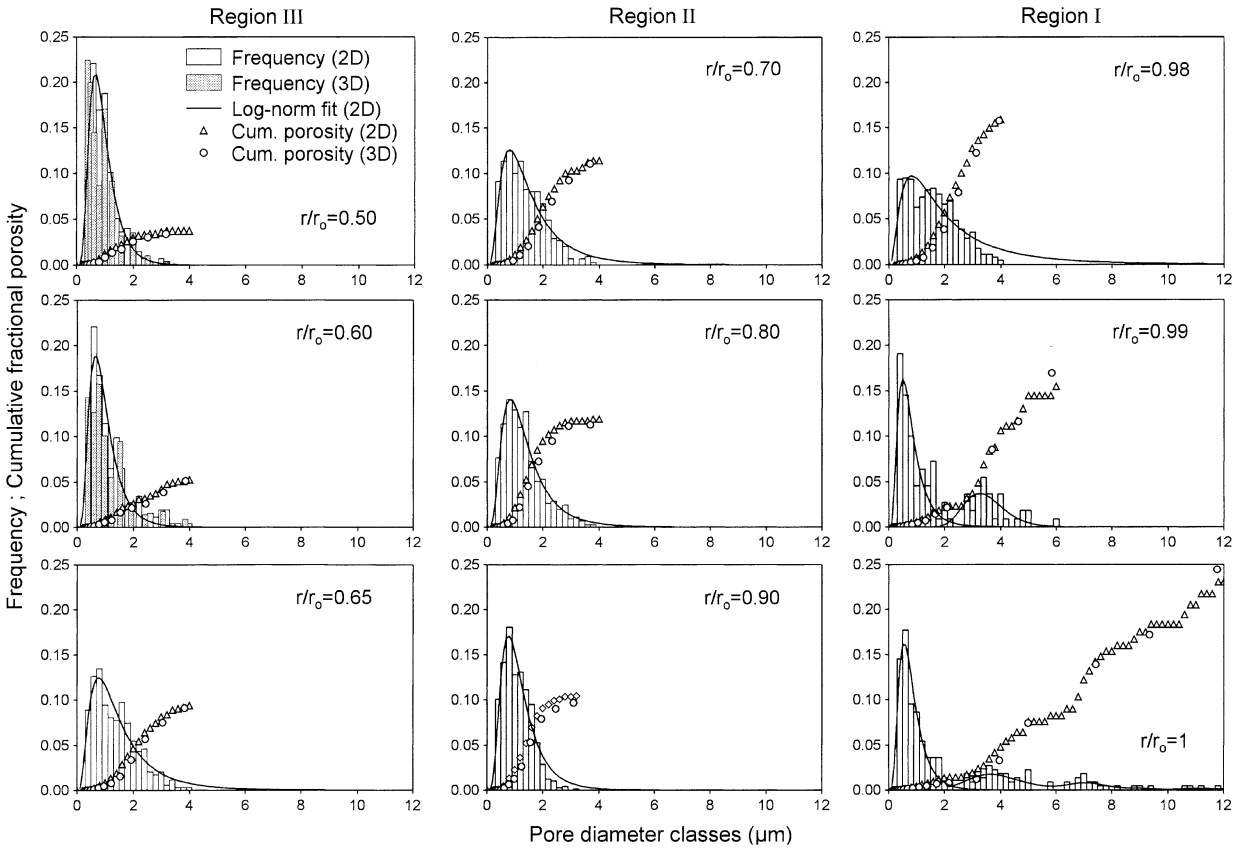

Fig. 4. Fuel with 98 GWd/tM average burn-up. Pore-size-distributions (frequency histograms) (2D, 3D) and corresponding cumulative porosity (2D, 3D) at different radial positions throughout regions I–III of Figs. 2 and 3.

4.5. Critical burn-up for pore coarsening in the rim region

To visualize possible critical local burn-up conditions associated with the pore coarsening process suggested in the former section for the fuel periphery, the 2D-porosity and 3D-pore density data of the fuel with 98 GWd/tM were plotted in Fig. 5 as a function of the local burn-up, considering only the values of region I (as from Figs. 2 and 3). The figure contains also values of other two fuels at the end of the fifth and seventh irradiation cycles, respectively, with 67 and 80 GWd/tM average burn-ups. For the first case data were taken from [1,22]. For the second case, as only values of porosity [22] and 2D-pore density (N_A) (unpublished results) were available, the corresponding 3D-pore density was estimated using the relations $D_P(2D) = (4P/\pi N_A)^{1/2}$ and $D_P(3D) = (6P/\pi N_V)^{1/3}$. The ratio $D_P(3D)/D_P(2D) = 1.12(\pm 0.12)$ was so employed as from [1] (work based on optical micrographs at 500× magnification). Data of the present work based on SEM-micrographs at magnification 1000×, showed $D_P(3D)/D_P(2D)$ ratios in the lower limit of the mentioned range (Table 2).

The results of Fig. 5(top and bottom) evidence a critical point on reaching the local burn-ups the value of ≈100 GWd/tM. At this point the pore density achieves a maximum and the porosity-growth-rate decreases. It is shown that after exhibiting a relatively high value for burn-ups in the range 60–100 GWd/tM (~1.7%/10 GWd/tM), at burn-ups above 100 GWd/tM the porosity-growth rate decreases and stabilizes at the level near ≈0.6%/10 GWd/tM (Fig. 6(top)). This value is close to the matrix-gas swelling-rate recently assessed in [8] for high burn-up fuels. More about this coincidence is treated in Section 5.

On the other hand, the maximum in the pore density achieved at about 100 GWd/tM (Fig. 5(bottom)) signals the onset of the pore coarsening process previously anticipated for the peripheral region I. This

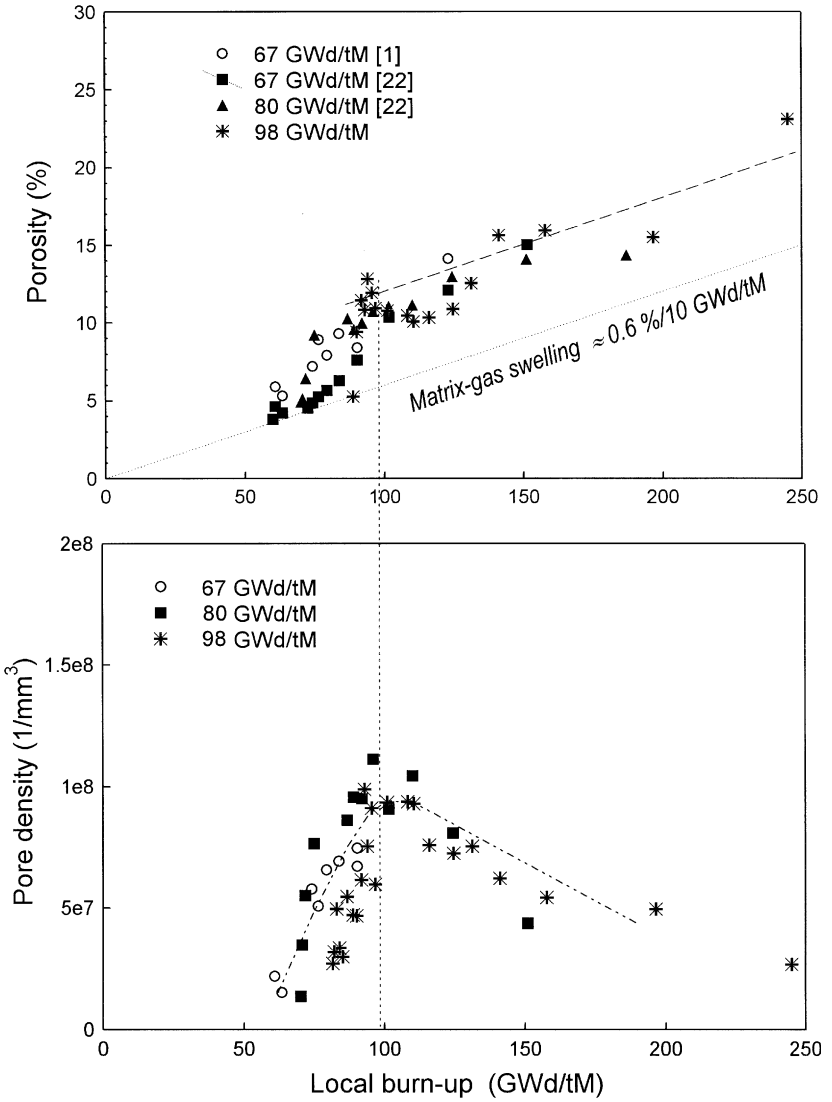

Fig. 5. 2D-porosity and derived 3D-pore density data for fuels with 67–98 GWd/tM average burn-ups (ends of fifth to ninth cycles) as a function of the local burn-up as calculated with the APOLLO 2 code.

can be better appreciated in Fig. 6 where both the 3D-pore-density and the 3D-mean-pore-radius are plotted in log–log mode as a function of the local burn-up (values in Table 2). As clearly seen in the figure, for burn-ups above ≈100 GWd/tM a sustained increase of the mean pore size is verified. It is noteworthy that in the previous work [1] on fuels at lower burn-ups, although a behaviour similar to that described here was not explicitly manifested, the remark was made that the maximum pore density did not occur at the pellet edge, but at a small distance from it. At these positions, the threshold discussed here was probably just reached.

Regarding the eventually applicable pore coarsening mechanism we remark that apart from the skewness of the size-distributions, treated in the previous section, another criterion of assignation is the cavity-growth kinetics. In fact studies demonstrate that the average cavity size increases proportionally to $t^{1/5}$ for processes of the coalescence type [18,23,24], whereas it does proportionally to $t^{1/2}$ for Ostwald-ripening [21,23,24]. Other coarsening process, as e.g. that driven by vapour transport, which leads to a pore-growth-kinetics proportional to $t^{1/3}$ [23,24], may be disregarded in the present case because of the low temperatures involved in the rim zone.

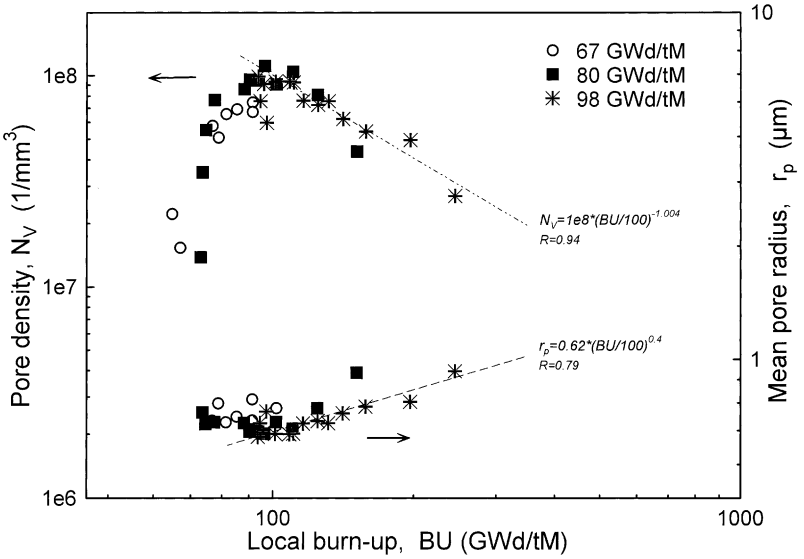

Fig. 6. 3D-pore density and corresponding 2D-average-pore-diameter data as a function of the local burn-up for fuels with 67–98 GWd/tM average burn-ups (ends of fifth to ninth cycles), in log–log plot. Local burn-ups according to APOLLO 2 code calculations.

Assuming the equivalence time ≡ burn-up, the data plotted in Fig. 6 (lower curve) suggest with reasonable precision a cavity-size-growth kinetics proportional to $t^{0.4}$ in region I (rim zone), after exceeding the critical burn-up of 100 GWd/tM. Thus, opposite to the above section, where the skewness of the pore-size distributions suggested a pore-coarsening by coalescence, the pore-size growth kinetics in this section indicates a coarsening process closer to Ostwald-ripening ($\propto t^{0.5}$ [21,23,24]).

Congruently, the kinetics of pore-density-drop after the maximum at 100 GWd/tM-burn-up is shown in Fig. 6(upper curve) to occur proportionally to t^{-1}. This coincides with the predicted t^{-1}-dependence of the drop of the number of precipitates in supersaturated solutions [20], or of (monoatomic) gas-filled pores in solids [25], both under conditions of ripening. For the coalescence case, a much slower pore-density-drop, namely proportional to $t^{-2/5}$ [18], is expected.

4.6. Pore-contact onset near the Chandrasekhar limit

Fig. 7 illustrates typical pore features of the fuel with 98 GWd/tM average burn-up within the previously defined regions I and II (Figs. 2–4). It can be seen that at radial positions $r/r_0 = 0.75$ and $r/r_0 = 0.83$ (the description is also valid for positions in between), repeated incipient pore-contact events are recognizable, showing overlapping of principally two pores. For radial position $r/r_0 = 1$, where pores appear ostensibly enlarged, the contours of the cavities frequently indicate previous conjunction of (generally two) smaller pores (Fig. 7). Figs. 2 and 3 clearly show that these radial positions are associated with porosity fractions at and above the threshold of ~0.1. For porosity fractions below 0.1, no noticeable pore-contact events were observed. Figs. 5 and 6 indicate also clearly that above this threshold pore-density-drop and pore coarsening take place. Thus, in conflict with the kinetics results of the above section, it is shown in the following that the value of this threshold is consistent with the hypothesis of pore growth caused by coalescence.

In the former sections we quoted that coalescence [18,19] and Ostwald-ripening [20,21] are the main mechanisms proposed in the literature for the coarsening of gas-cavities in solids. The first process applies when cavity mobility is important [19]. In fact, as formulated first by Gruber [26], the theory of bubble coarsening by migration and coalescence (M&C), based by analogy in the treatment of random walk and colloids coagulation of Chandrasekhar [27], assumes bubbles to migrate by surface diffusion and to coalesce unrestrictedly upon contact [24,26]. However, alone the hypothesis of cavity mobility would make the M&C-treatment inapplicable for the large 1 μm-size rim-pores (gas-bubbles in UO_2 with diameters >2 nm had been considered historically to be virtually immobile at temperatures below 1500 °C [28,29]). We shall keep in mind this contradiction.

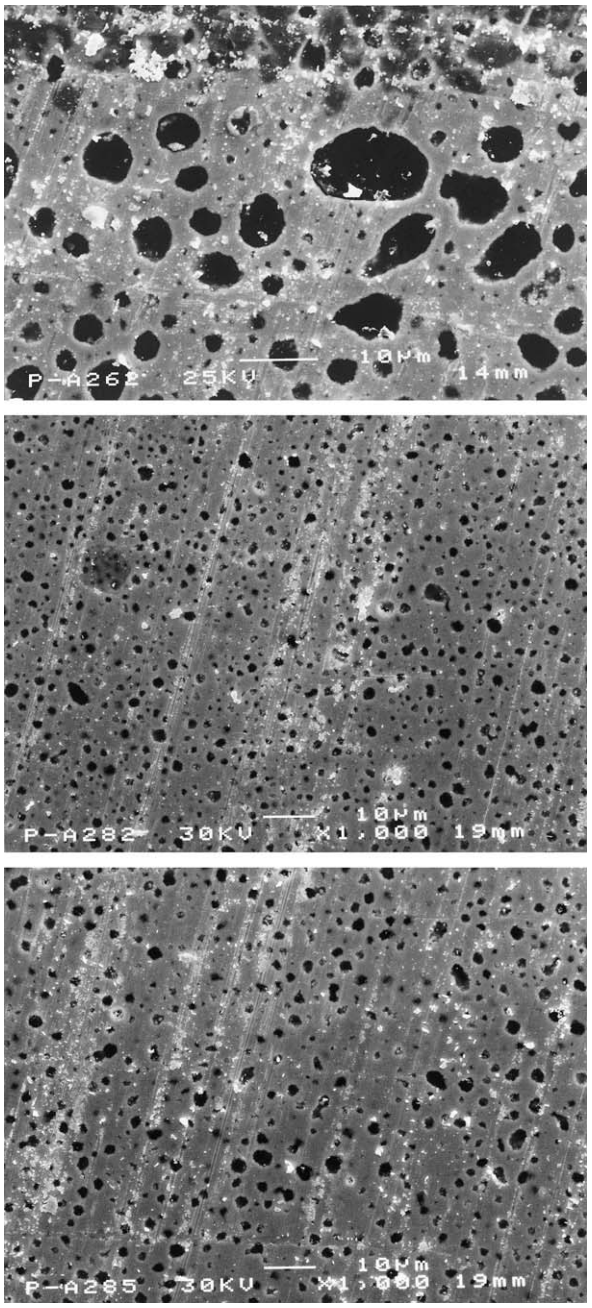

Fig. 7. Fuel with 98 GWd/tM average burn-up. Typical microstructure features evidencing pore contact and pore coarsening throughout regions I and II of Figs. 2 and 3. Top: $r/r_0 = 1$; middle: $r/r_0 = 0.83$; bottom: $r/r_0 = 0.75$.

Chandrasekhar formulae [27], which apply to a number of cases from colloids coagulation to stellar dynamics, deal with stochastic processes in a system of n spatially uncorrelated (i.e. random) 'point particles' following a Poisson distribution [30,31]. Of this system, the number of collisions per unit time (coalescence rate) was taken by Gruber in [26] to construct the M&C-formalism. Another characteristic number of this system is the nearest-neighbour distance, which was found by Chandrasekhar in [27] to be $\lambda = \Gamma(4/3)(4/3\pi N_V)^{-1/3}$ (Γ is the gamma-function and N_V is the volume-concentration of particles). Assuming the size of the particles (or voids) to be narrowly distributed around an average diameter D, the Chandrasekhar nearest-neighbour-distance results: $\lambda_{\text{Chandr.}} = D0.5\Gamma(4/3)\phi^{-1/3}$ ($\phi =$ particle (or void) fraction, $D = (6\phi/\pi N_V)^{1/3}$). Statistically seen, contact between particles would then occur when the average diameter of the particles exceeds the nearest-neighbour distance ($\lambda/D \leqslant 1$), i.e., for $\phi \geqslant 0.089$.

We note that a similar assumption as the above was done recently by White [33] for the grain-face porosity in irradiated oxide fuels, deriving cavity-contact to occur at area coverage (ϕ_A) $\geqslant 0.196$. As in two dimensions is $\lambda_{\text{Chandr.}} = \Gamma(3/2)(\pi N_A)^{-1/2}$ [10,32], $N_A = 4\phi_A/\pi D_A^2$ is the area-concentration of particles (voids) and D_A is the average projected diameter in the surface, the deduction in [33] is straightforward.

However, the above treatment can be applied to discrete particles only for small sizes (i.e., small particle fractions) (dilute limit) [31,32]. For the general case, the exact solution of the nearest-neighbour distance in a system of random penetrable (or Poisson distributed) spheres of size D, is due to Torquato [31], who found this being $\lambda = 0.5D\Gamma(4/3)[\ln(1-\phi)^{-1}]^{-1/3}$; all quantities having the same meaning as before defined. This function is plotted in Fig. 8 together with that of Chandrasekhar (dilute limit). As can be seen, for small particle fractions both curves are coincident. The exact solution due to Torquato [31] predicts $\lambda/D \leqslant 1$ situations to occur at slightly smaller particle fractions compared to the Chadrasekhar-limit ($\phi \geqslant 0.089$), i.e., at $\phi \geqslant 0.085$ (Fig. 8).

As also marked in Fig. 8, the pore-contact threshold verified experimentally at porosity fractions between 0.10 and 0.11 occurs very near the above ($\lambda/D \leqslant 1$)-limit predicted for an idealized system of random penetrable mono-sized spherical cavities. The light shift to higher cavity fractions may be explainable from departures of the assumed ideal conditions. In fact, in the real case of our interest (rim zone), pores are obviously not single-sized (Section 4.4, Fig. 4), and may be not perfectly spherical and not fully randomly distributed; the latter recognizing that certain spatial correlation between

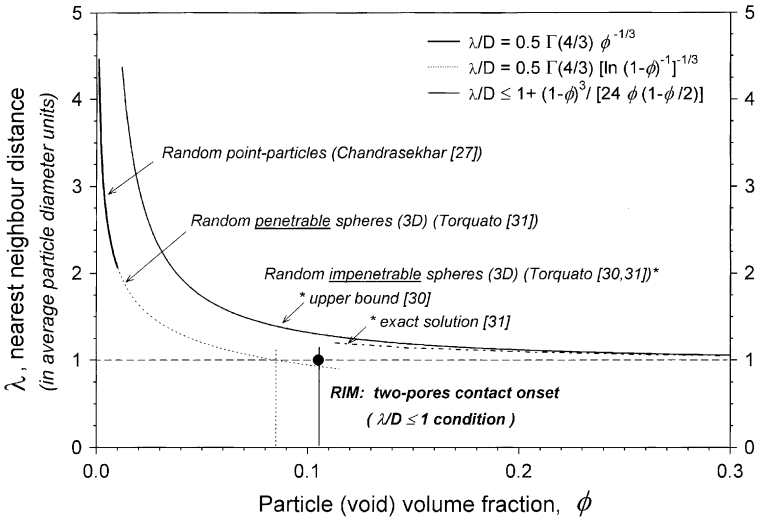

Fig. 8. Nearest-neighbour-distance functions for the model systems of random point particles [27] and random penetrable and impenetrable discrete-size spheres [30,31] as a function of the particle (or void) fraction. Nearest-neighbour-distance expressed in units of the average particle diameter.

the pores and the underlying subgrain structure may exist e.g. via nucleation of cavities at preferential sites like triple-point junctions [34].

For heterogeneous materials, an increasing spatial correlation between particles of a dispersed phase (pores in our case) is described in [31] as causing an increasing impenetrability of the particles (i.e., appearance of exclusion-zones around particles), which in general leads to an increase of their nearest-neighbour distance [31,35]. For the limit case of fully impenetrable spheres of size D, Fig. 8 illustrates the nearest-neighbour-distance function as determined by Torquato in [30] (upper bound) and [31] (exact solution). These curves predict $\lambda/D \leqslant 1$ situations at particle (void) fractions above 0.3. It is then ostensible that the experimental pore-contact threshold is much closer to the predicted $\lambda/D = 1$ limit for the penetrable case ($\phi \approx 0.085$). These results indicate that, at least geometrically, rim pores can be seen as penetrable (quasi-spherical) entities that would be able to grow in size on contact (i.e., by coalescence or conjunction), in principle, on exceeding cavity fractions of $\phi \approx 0.1$. The remaining question is whether this could occur in case of restricted mobility of the cavities.

4.7. Percolation threshold as from minimum-solid-area curves

In Ref. [6] we have used by first time minimum-solid-(or load-bearing)-area functions to fit the hardness vs. porosity curves of the rim and the as-sintered UO_2 materials, in an attempt to assign model systems to both materials, for anticipating values of their percolation thresholds. As regard to values of the rim zone, data in [6] were well fitted by a function of the type e^{-bP} with $b = 2.31$ (P = porosity fraction), indicating similar (or somewhat stiffer) behaviour as for the system of cubic-packed spherical pores, for which it holds $b \approx 3$ [6,36], and whose percolation threshold is $\phi_c = 0.524$ [6,36]. However, as the occurrence of such fully ordered configuration of voids appears improbable, the random version of the model, namely overlapping spherical pores in a matrix, was tentatively assigned to the rim [6]. For such a system, which is the same as the previously described in Section 4.6 ('fully penetrable spheres'), and which according to [31] is also called 'spatially uncorrelated spheres', 'Poisson distributed spheres' or simply the 'Swiss-cheese model' (obvious name when spheres are replaced by voids), the percolation threshold is $\phi_c = 0.2895 \pm 0.0005$ [31].

Substantiating the above, the hardness results of [6] (average burn-ups $\leqslant$80 GWd/tM), and those of Fig. 2(bottom) of the present work (average burn-up $\approx$98 GWd/tM), are re-plotted in Fig. 9 as a function of porosity, together with the curve $H/H_0 = (1 - (P - P_0)/0.818)^{1.65}$, which represents the load-bearing-area of the system of overlapping pores. This last curve was taken from the E/E_0 vs. P values computed for this system in [37], assuming

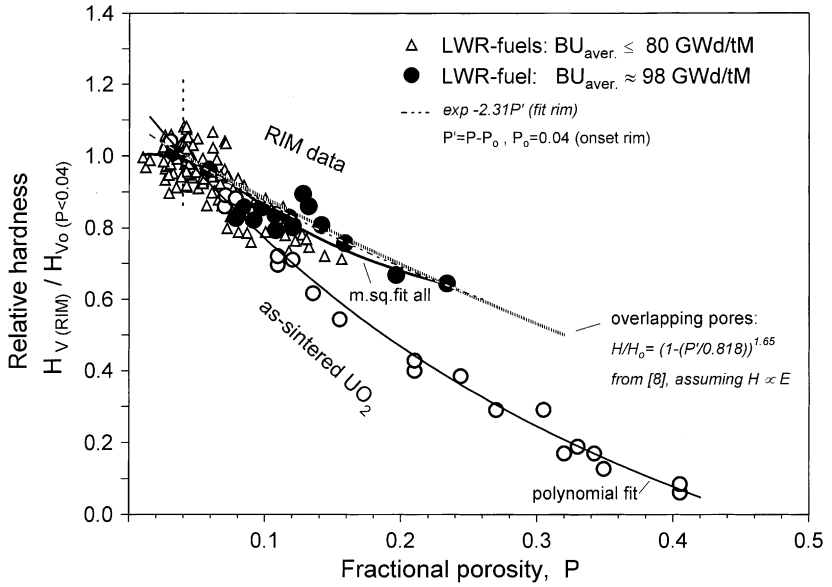

Fig. 9. Relative fuel hardness and minimum-solid-area-curves (fractional bearing area) as a function of porosity for unirradiated UO_2 and irradiated PWR-fuels with maximum 98 GWd/tM average burn-ups.

proportionality between hardness and *E*-modulus. It is seen that the last curve matches the results of the rim as good as the previously mentioned exponential function did. Using this system to describe the rim, and fixing tentatively its percolation threshold at $\phi_c = 0.3$, appears therefore justified. As for the results of the non rim-transformed fuel (as-received structure), also shown in Fig. 9, the analysis remain the same as in [6], notably indicating less stiff behaviour and much lower associated percolation threshold as compared to the rim material.

As remarked in the previous section, some degree of correlation (impenetrability, exclusion-volume effects) is likely to occur for the rim system, which would also make its percolation threshold to rise [31,35]. The penetrable sphere model (Swiss-cheese) would thus represent the *lower bound* for the rim material, both in terms of the nearest-neighbour distance between pores and the percolation threshold.

4.8. Grain size evolution throughout the fuel radius

Apart from the porosity changes (former sections), another important marker of processes occurring across the fuel radius is the grain size evolution in the restructured zones. However, as for evidence in the literature, there appear to be no significant changes of this parameter neither vs. important variations of temperature nor of the fission rate [38,39]. Indeed, in the particular fuel of [38,39], for which the rim structure penetrated considerably into the fuel (to $r/r_0 \approx 0.74$), constant grain size histograms, similar to that previously found by us in [1] (i.e., centred at 0.3 μm), were observed across the whole rim region, although the assigned temperatures varied between 400 and 1100 °C and the fission rates between 1 and 5×10^{13} f/cm^3 s [38,39].

For the fuel analysed in the present work the situation is different. As shown in Fig. 10, a modification of the grain- and related pore-structure appears visible when moving from regions I to III of the fuel radius (regions marked in Figs. 2 and 3). The first important remark from Fig. 10 is that the faceted nature of the pores (typical of region I) appears to gradually disappear when moving towards central positions. At the inner end of region II and in region III, pores appear to acquire a triple-point-like morphology and the size of the surrounding (sub)grains increases, as particularly seen at $r/r_0 = 0.55$ (region III) (Fig. 10). Another remark is that the typical characteristic of the rim pores, showing generally a finer grain structure at their inner face [1,39], tends to also disappear in region III.

The corresponding grain size distributions for each micrograph of Fig. 10 (whole field) are shown in Fig. 11. The figure shows also the histogram of the rim zone measured previously in [1]. For comparison, also the corresponding local burn-ups and

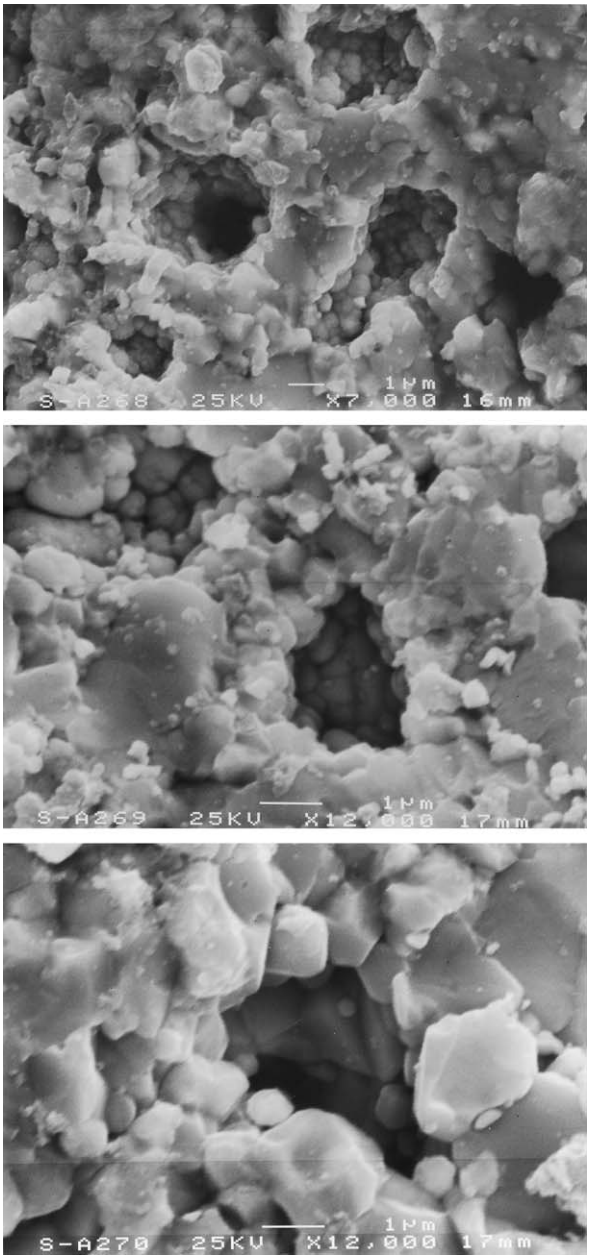

Fig. 10. Fuel with 98 GWd/t M average burn-up. Pore and recrystallized-grain features in regions I–III of Figs. 2 and 3. Top: $r/r_0 = 1$; middle: $r/r_0 = 0.7$; bottom: $r/r_0 = 0.55$. From regions II and III towards the fuel centre: increasing number of triple point-like pores. In region I (pure rim-zone): dominantly faceted pores. Note conjunction of two pores (peanut-like cavity) at the pellet-edge micrograph (top).

the local temperatures (as from Fig. 1) are assigned to each histogram of the figure. It can be seen that at the pellet edge positions, both fuels with 67 and 98 GWd/tM average burn-ups, exposed to similar outer irradiation temperatures (respectively, 381 and 374 °C), presented similar grain size distributions (i.e., peaked at 0.3 μm); though somewhat wider for the case of the higher burn-up (Fig. 11). The fuel with 98 GWd/tM average burn-up at radial position $r/r_0 = 0.7$ shows however much wider size distribution than at the pellet edge, with an increased median grain size of 0.4–0.5 μm. For the same fuel, the histogram at radial position $r/r_0 = 0.55$ shows ostensible widening (grain-growth); the median grain size is placed somewhat above 0.6 μm, i.e., at double the size that at the pellet edge (Fig. 11).

It is certainly difficult to find explanations why for the fuel here examined (Figs. 10 and 11) the grain size at the hotter front of the recrystallization zone ($r/r_0 = 0.55$, $T \approx 812$ °C) increased by a factor 2 respect that of peripheral positions; and why for the fuel of Refs. [38,39], for which the equivalent front experienced much higher temperatures ($r/r_0 = 0.73$, $T^{\max} \approx 1200$ °C) [38], it did not. According to Fig. 1, the temperatures of the present fuel were the lowest at the end the fifth cycle. At this stage of the irradiation the rim-zone was probably only 200–250 μm wide [1], so that at position $r/r_0 = 0.55$ the grain structure was still the original one. Between the fifth and the ninth cycle, where the zone in question may have been recrystallized, the local temperatures varied between 760 and 812 °C (Fig. 1). At these moderate temperatures it is hard to imagine that a pure thermally activated secondary recrystallization (i.e., grain growth) would have occurred in addition to primary recrystallization. Grain growth in the recrystallized region has been recently shown to not occur (out-of-pile) on ramp heating up to temperatures of 1800 °C [41]. More complex diffusional process may had been therefore present.

5. Discussion

The main objective of this work has been to study trends in the stereological parameters (i.e., pore- and related grain-structure) associated with the high burn-up transformation in the periphery of LWR-fuels, when fuels are irradiated up to the ninth cycle and beyond. As seen in the results section, one of the consequences of the prolonged irradiation is the light elevation of the temperatures in the outer half-pellet-radius due to thermal conductivity deterioration, in our case, after the fifth cycle. Under these conditions, we observed that apart from the rim-transformation, a second restructuring process,

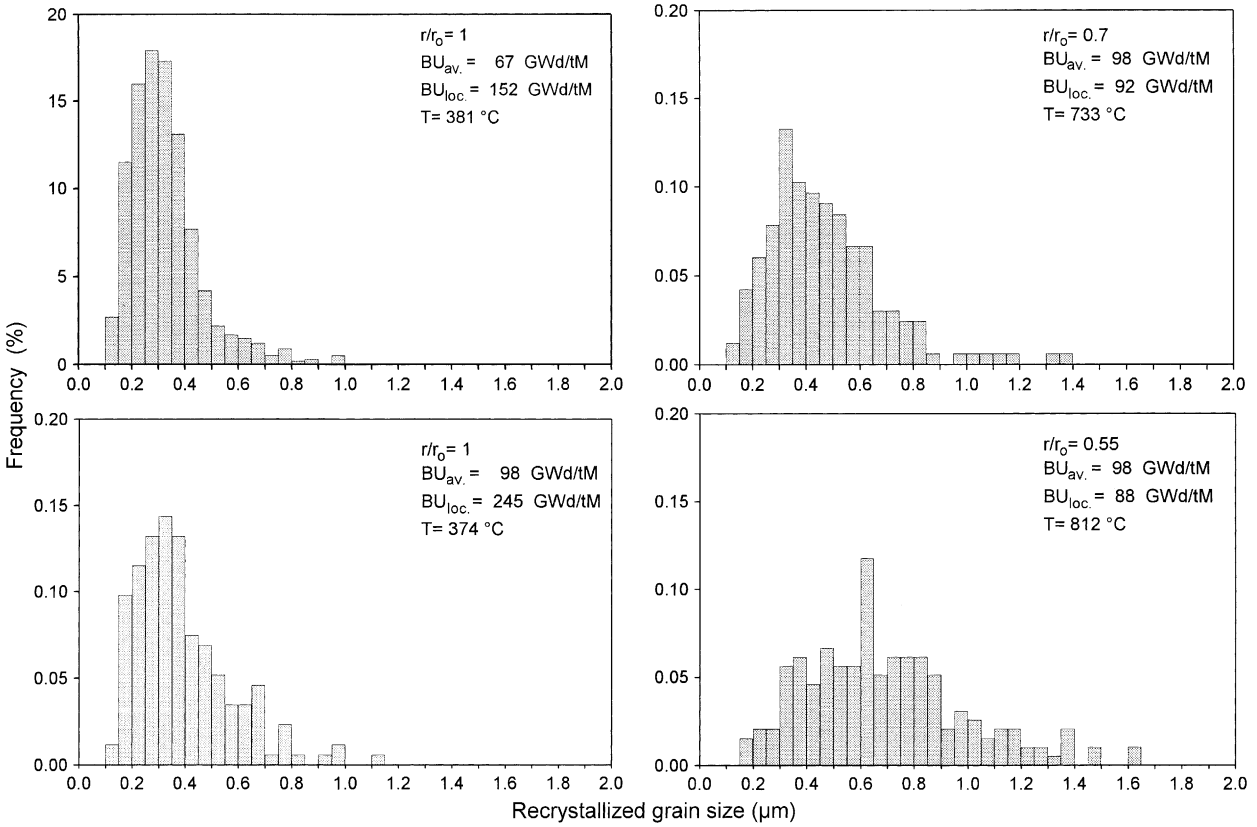

Fig. 11. Fuel with 98 GWd/tM average burn-up. Grain size distributions of the recrystallized fields shown in Fig. 10 ($r/r_0 = 1$, 0.7 and 0.55). Comparison with grain size distribution at the pellet edge of the fuel with 67 GWd/tM average burn-up (end of fifth cycle).

eventually rim-like, was established at positions around $r/r_0 \approx 0.7$, tentatively from the seventh irradiation cycle onwards. This caused additional elevation of the local porosity and decrease of the local fuel hardness. However, the constancy of the pore density, and the verified (sub)grain growth, instead of the expected extra grain subdivision, allow disregarding this process as rim-like. More likely, the changes are to be attributed to thermally activated mechanisms superimposed to the extending rim-transformation. The mentioned light temperature increase in this, so-called, transition region would have played a role in this respect.

However, the main processes herein of interest are those occurring in the fuel periphery (region I). In this a-thermal, burn-up dominated region, the most remarkable finding in this work is the pore coarsening and pore-density decrease, which is verified upon exceeding local burn-ups of ≈100 GWd/tM, or, on exceeding porosity fractions of ≈10% (Section 4.5). Since these values may be dependent upon the external mechanical restraint (coolant pressure) cross-check tests with other fuels under different irradiation conditions may be necessary. Interesting to note is, however, that above this critical threshold the slope of porosity-growth falls and stabilizes at the constant value near ≈0.6%/10 GWd/tM, which is close to the matrix-gas swelling-rate assessed by us in [8] for high burn-up fuels. As emphasized in [8], for high burn-up fuels the matrix swelling caused by fission gases is gradually converted into porosity at the time that Xe-gas gets expelled from the lattice, a processes which is seemingly quite completed at local burn-ups around 120 GWd/tM [8]. Above this tentative limit all volume increase attributable to fission gases would be found in the fuel in form of porosity [8], which may be consistent with the porosity growth trend confirmed in the present work after the threshold.

An important feature of the pore coarsening in region I is the associated decrease of the pore-number. As mentioned repeatedly in former sections, pore-size increase in concomitance with pore-number-drop let interpreting the cavity growth as caused

either by coalescence or ripening. The first case implies usually cavity migration and unification after contact [18,19,23,24]; the second one assumes cavities to be not necessarily mobile and remaining separated by a minimum distance smaller than their mean linear dimension [20]; growing the larger ones at expense of the smaller ones, which finally disappear. In the last, the driving force is due to concentration gradients of the segregating species from the supersaturated matrix, near the cavity surface [20,21,25].

Unfortunately, the process in the rim region could not be exclusively attributed to one or the other of the above mechanisms; the experimental evidences showed this having ingredients of both model cases. Thus, from the one hand, the skewness of the pore size distributions (log–norm type) (Section 4.4) and the proximity of the porosity-threshold for pore coarsening (≈0.1–0.11) with the Chandrasekhar-like limit for cavity contact ($\phi \geqslant 0.089$) [27,30,31] (Section 4.6) suggested pore growth by coalescence. On the other hand, the kinetics of pore-size-growth ($\propto t^{0.4}$) and pore-density-decrease ($\propto t^{-1}$) strongly suggested pore coarsening by ripening, for which it holds, respectively, proportionality with $t^{0.5}$ [21,23,24] and t^{-1} [20,25] (Section 4.5).

Occurrence of overlaid coalescence and ripening mechanisms, as it could be the case for the rim-pores, has been proposed by Ronchi [40] to explain different aspects of the gas-bubble swelling in MX-type nuclear fuels. The difference with the present case is that bubbles in [40] were indisputably mobile because of their small size (nm-range), therefore validating the assumption of coalescence on contact. This is certainly not the case of the rim-pores (μm-range). The same occurred in the case of the grain-face porosity in ramped nuclear fuels recently analysed by White [33], where a geometrical coalescence criterion similar to that of Section 4.6 was employed. In [33], despite bubbles achieved partially also relatively large sizes (sub μm- and μm-range), the temperatures were comparatively much higher (>1500 °C), such that cavity mobility by surface diffusion was possible. Indeed, the derived bubble diffusion coefficient in [33] was consistent with previous values of surface diffusion coefficients in UO_2.

The tacit requirement of cavity migration is certainly the weakest point of the coalescence-like criteria derived in Sections 4.4 and 4.6 for the rim pores. However, the morphology of these cavities after the porosity threshold (⩾0.1–0.11) let few doubts about pore conjunction (unification) taking place after contact (see particularly Fig. 7(top) and Fig. 10(top)). We recall here the work by Evans [19] on He-implanted silicon, where this kind of observation (elongated cavities) was referenced as criterion for coalescence. Also, the proximity of the experimental pore-contact onset with the nearest-neighbour-distance criterion derived for model system of random *penetrable* discrete spheres (Chandrasekhar-like, Swiss-Cheese model) [30,31] (Section 4.6), allows assuming cavity unification on contact. On the other hand, the assumption of pure random distribution of rim-cavities appears not fully realistic, as certain spatial correlation between the pore system and the underlying (sub)grain structure [34] may exist (Section 4.6). Certainly, an adequate theory for the creation and evolution of the rim porosity, contemplating all complex aspects herein described, is lacking.

We turn back to one of the primary goals of the work as expressed in the introduction, attempting to visualize limits of gas retention for the rim structure as from its stereological evolution. In this sense, we find important the evidence in Sections 4.6 and 4.7 showing the system of random *penetrable* spheres (Swiss-Cheese-Model) [30,31], with proved pore-connectivity limit at $\phi_c = 0.2895 \pm 0.0005$ [31], to represent the *lower bound* for the rim-material both in terms of the nearest-neighbour distance between pores and the percolation threshold [35]. In this sense, it is important to remark the lack of pore interconnection verified previously by us for the present fuel on optical 3D-tomographs of regions with up to ≈24% porosity [7]. This allows stating that the percolation threshold, which is normally associated with the formation of long-chains (clusters) of interconnected pores [31], absent here, is still far from this porosity level. Closure of the rim-pores tentatively up to void-fractions of the order of 0.3 seems therefore plausible.

Nevertheless, the question arises as to whether the here disregarded inter-granular gas-bubbles, observed in the rim-material by TEM examinations [42], could form a network of grain-boundary channels that enables interconnection of large cavities (pores), supporting thus gas release from this region. By scaling-down the recent analysis of White [33] on grain-face porosity of irradiated fuels to the dimensions of the rim-grains, one would expect effective venting of (or via) grain-face cavities to occur only at large fractional surface coverage, e.g. 30% or higher, which implies a volumetric

swelling of ≈1–2% [33]. However, to the knowledge of the authors such a high level of grain-face decoration has never been verified on freshly-fractured rim-grains, at least not according to published data. Therefore, given the current experimental evidence, the conclusion can be drawn that venting of large cavities in the rim zone via grain boundary channels will be negligible under normal operation conditions. As corroborated in recent experimental work [41] and as anticipated in previous theoretical estimations [43], considerable gas release from this area would only occur under very fast transient conditions (e.g. RIA), namely on the base of additional mechanisms such as inter-granular fracturing.

The final point deserving attention is the sub-grain-size growth verified in the present work on moving within the rim-transformed zone towards inner fuel regions, exposed only to moderate temperatures of $T \approx 800$ °C. As expressed in Section 4.8, this opposes to previous results in the literature indicating invariability of the recrystallized grain size against drastic increase of the irradiation temperature up to 1200 °C [38,39]. It opposes also to recent evidence showing invariability of the grain size against rapid (out-of-pile) ramp heating up to 1800 °C [41]. The explanation of these discrepancies, which is out of the scope of the present work, opens certainly new areas of interest, as for instance the study of the combined (temperature, burn-up, fission rate)-conditions under which a secondary recrystallization (grain growth) in the rim zone is possible to take place.

6. Conclusions

The stereology of the rim-structure was studied for PWR-fuels up to the ninth irradiation cycle, achieving maximum local burn-ups of 240 GWd/tM and beyond. At intermediate radial positions ($0.55 < r/r_0 < 0.7$), slight increase of the pore and grain size of recrystallized areas was found, which is attributed to the increase of the irradiation temperatures in the outer half-pellet-radius due to deterioration of the thermal conductivity.

In the pure burn-up controlled rim-zone, marked pore coarsening and pore-density-decrease occur on surpassing the local burn-up of 100 GWd/tM, associated with cavity fractions of ≈0.1. Above this threshold the slope of porosity growth drops and stabilizes at a value near the rate of matrix-gas swelling, i.e., ≈0.6%/10 GWd/tM. From these limits onwards, the observed cavity coarsening shows ingredients of both Ostwald-ripening and coalescence mechanisms. As for the measured burn-up dependence of the average pore size and pore-density, respectively, $BU^{0.4}$ and BU^{-1}, they coincide fairly well with those of Ostwald-ripening (respectively, $t^{0.5}$ and t^{-1}, $BU \equiv t$). In contrast, the morphology of the pores, the limiting porosity for onset of pore growth and the positive skewness of the pore-size-distributions, probably indicate a coarsening process of the coalescence type. Here, however, contradiction arises with the tacitly implied pore mobility, which is not applicable to the (large size) rim-pores.

Despite pore coarsening and individual pore-contact events, formation of clusters of interconnected pores, a sign of proximity to the percolation threshold, was not verified up to the maximum studied void-fractions (≈0.24). The rim-structure is also found to be well represented in its lower bound by the model system of penetrable spheres (Swiss-Cheese), for which the percolation threshold is $\phi_c \approx 0.29$. Pores in the rim-material are thus expected to remain closed at least up to this limit.

Acknowledgement

The authors would like to thank Professor Salvatore Torquato, Department of Chemistry, Institute for Science and Technology of Materials, and Program in Applied and Computational Mathematics, Princeton University, NJ, USA, for invaluable discussions and suggestions on applicable theoretical models of dispersed phases in heterogeneous materials. The authors are indebted also to the Nuclear Power Station Gösgen, Switzerland, for the possibility to use their unique high burn-up fuel material for the present studies.

References

[1] J. Spino, K. Vennix, M. Coquerelle, J. Nucl. Mater. 231 (1996) 179.
[2] K. Une, M. Hirai, K. Nogita, T. Hosokawa, Y. Suzawa, S. Shimizu, Y. Etoh, J. Nucl. Mater. 278 (2000) 54.
[3] J. Rest, G.L. Hofman, in: Proceedings of the Materials Research Society Meeting, Symposium R, Boston, MA, November 2000.
[4] N. Lozano, L. Desgranges, D. Aymes, J.C. Niepce, J. Nucl. Mater. 257 (1998) 78.
[5] J. Spino, D. Baron, M. Coquerelle, A. Stalios, J. Nucl. Mater. 256 (1998) 179.
[6] J. Spino, J. Cobos-Sabate, F. Rousseau, J. Nucl. Mater. 322 (2003) 204.

[7] J. Spino, D. Papaioannou, J.-P. Glatz, J. Nucl. Mater. 328 (2004) 67.
[8] J. Spino, J. Rest, W. Goll, C. Walker, J. Nucl. Mater. 346 (2005) 131.
[9] R. Manzell, C.T. Walker, in: Proceeding of the ANS International Topical Meeting on LWR Fuel Performance, ANS, Park City, Utah, 2000, p. 604.
[10] E.E. Underwood, Quantitative Stereology, Addison-Wesley Publishing Company, 1970.
[11] P. Magat, A. Nicholas, I. Zmijarevic, G. Mothonnière, H. Golfier, C. Poinot-Salomon, P. Marotte, C. Bangil, PHYSOR 2000, May 2000.
[12] C. Callu, D. Baron, J.-M. Ruck, in: International Conference on Candu Fuel, Toronto, Canada, September 21–25, 1997.
[13] D. Baron, B. Lhermitte, J.-P. Piron, IAEA Technical Committee Meeting on Advances in Pellet Technology for Improved Performance and High Burn-up,Tokyo, Japan, 26 October–1 November 1996.
[14] P.E. Mac Donald, J. Weisman, Nucl. Technol. 31 (1976) 357.
[15] B. Schulz, High Temp.–High Press. 13 (1981) 649.
[16] C. Ronchi, M. Sheindlin, D. Staicu, M. Kinoshita, J. Nucl. Mater 327 (2004) 58.
[17] H. Assmann, R. Manzel, J. Nucl. Mater 68 (1977) 360.
[18] V. Zell, H. Trinkhaus, H. Schroeder, J. Nucl. Mater. 212–215 (1994) 320.
[19] J.H. Evans, Nucl. Instrum. and Meth. B 196 (2002) 125.
[20] I.M. Lifshitz, V.V. Slyozov, J. Phys. Chem. Solids 19 (1961) 35.
[21] P.F.P. Fichtner, H. Schroeder, H. Trinkhaus, Acta Metall. Mater. 39 (1991) 1845.
[22] J. Spino, D. Papaioannou, J. Nucl. Mater. 281 (2000) 146.
[23] S.K. Tyler, P.J. Goodhew, J. Nucl. Mater 92 (1980) 201.
[24] P.J. Goodhew, S.K. Tyler, Proc. R. Soc. Lond. A 377 (1981) 151.
[25] A.J. Markworth, Metall. Trans. 4 (1973) 2651.
[26] E.E. Gruber, J. Appl. Phys. 38 (1967) 243.
[27] S. Chandrasekhar, Rev. Mod. Phys. 15 (1943) 1.
[28] J.A. Turnbull, J. Nucl. Mater. 62 (1976) 325.
[29] C. Baker, J. Nucl. Mater. 71 (1977) 117.
[30] S. Torquato, Phys. Rev. E 51 (1995) 3170.
[31] S. Torquato, Random Heterogeneous Materials – Microstructure and Macroscopic Properties, Springer, 2002.
[32] R.T. DeHoff, F.N. Rhines, Quantitative Microscopy, McGraw-Hill Book Company, 1968.
[33] R.J. White, J. Nucl. Mater. 325 (2004) 61.
[34] J. Rest, J. Nucl. Mater. 326 (2004) 175.
[35] S. Torquato, personal communication, 2005.
[36] R.W. Rice, Porosity of Ceramics, Marcel Dekker, 1998.
[37] A. Roberts, E.J. Garboczi, J. Am. Ceram. Soc. 83 (2000) 3041.
[38] M. Kinoshita, T. Kameyama, S. Kitajima, Hj. Matzke, J. Nucl. Mater. 252 (1998) 71.
[39] I.L.F. Ray, Hj. Matzke, H.A. Thiele, M. Kinoshita, J. Nucl. Mater. 245 (1997) 115.
[40] C. Ronchi, J. Nucl. Mater. 84 (1979) 55.
[41] K. Une, S. Kashibe, A. Takagi, in: Proceedings of the 2005 Water Reactor Fuel Performance Meeting, Kyoto, Japan, October 2–6, 2005, 978, ISBN 4-89047-132-4.
[42] L.E. Thomas, C.E. Beyer, L.A. Charlot, J. Nucl. Mater. 188 (1992) 80.
[43] J. Rest, G.L. Hofman, J. Nucl. Mater. 223 (1995) 192.